Core structure of two-dimensional Fermi gas vortices in the BEC-BCS crossover region

Lucas Madeira,[1,*] Stefano Gandolfi,[2] and Kevin E. Schmidt[1]
[1]*Department of Physics, Arizona State University, Tempe, Arizona 85287, USA*
[2]*Theoretical Division, Los Alamos National Laboratory, Los Alamos, New Mexico 87545, USA*
(Received 7 March 2017; published 2 May 2017)

We report $T = 0$ diffusion Monte Carlo results for the ground-state and vortex excitation of unpolarized spin-1/2 fermions in a two-dimensional disk. We investigate how vortex core structure properties behave over the BEC-BCS crossover. We calculate the vortex excitation energy, density profiles, and vortex core properties related to the current. We find a density suppression at the vortex core on the BCS side of the crossover and a depleted core on the BEC limit. Size-effect dependencies in the disk geometry were carefully studied.

DOI: 10.1103/PhysRevA.95.053603

I. INTRODUCTION

The study of cold Fermi gases has proven to be a very rich research field, and the investigation of low-dimensional systems has become an active area in this context [1,2]. Particularly, the two-dimensional (2D) Fermi gas has attracted much interest recently. It was the object of several theoretical investigations [3–8], but its experimental realization, using a highly anisotropic potential, was a milestone in the study of these systems [9]. Many other studies have been carried out since [10,11]. Quantum Monte Carlo (QMC) methods were successfully employed to compute several properties of the BEC-BCS crossover. These methods include diffusion Monte Carlo (DMC) [12,13], auxiliary-field quantum Monte Carlo [14], and lattice Monte Carlo [15–17]. The fact that a fully attractive potential in 2D always supports a bound state, and the ability to vary the interaction strength over the entire BEC-BCS crossover regime offers rich possibilities for the study of these systems.

The presence of quantized vortices is an indication of a superfluid state in both Bose and Fermi systems. In three-dimensional (3D) systems, much progress has been made [18–21], including the observation of vortex lattices in a strongly interacting rotating Fermi gas of ^{6}Li [22]. With the recent progress on the 2D Fermi gases, it seems natural to also extend the theoretical study of vortices to these systems. Interest is further augmented in 2D, where a Berezinskii-Kosterlitz-Thouless transition [23,24] could take place at finite temperatures, and pairs of vortices and antivortices would eventually condense to form a square lattice [25].

We are interested in how the properties of a vortex change over the BEC-BCS crossover. In this work we focus on ultracold atomic Fermi gases, but it is noteworthy that a duality is expected between neutron-matter and superfluid atomic Fermi gases. In 3D, both ultracold atomic gases and low-density neutron matter exhibit pairing gaps of the order of the Fermi energy [26]. Neutron-matter properties depend on the interaction strength and, unlike the Fermi atom gases, the possibility of microscopically tuning interactions of neutron matter is not available. However, we can study neutron pairing by looking at the BCS side of the crossover [27,28]. Vortex properties are also of significant interest in neutron matter [29,30] because a significant part of the matter in rotating neutron stars is superfluid, and vortices are expected to appear. Moreover, phases called nuclear pasta, where neutrons are restricted to 1D or 2D configurations, are predicted in neutron stars [30,31].

We report properties of a single vortex in a 2D Fermi gas. We considered the ground state to be a disk with hard walls and total angular momentum zero, and the vortex excitation corresponds to each fermion pair having angular momentum $\hbar$. Hopefully, our results will motivate experiments to increase our understanding of vortices in 2D Fermi gases.

This work is structured as it follows. In Sec. II we introduce the methodology employed. In Sec. II A we discuss aspects of finite-size fermionic systems, we briefly introduce 2D scattering in Sec. II B, Sec. II C is devoted to the wave functions employed for the bulk, disk, and vortex systems, and we summarize the employed QMC methods in Sec. II D. The results are presented in Sec. III. Section III A contains the ground-state energies in the disk geometry and discussions on size effects. In Sec. III B we present the vortex excitation energy. The determination of the crossover region is done in Sec. III C. Density profiles of the vortex and ground-state systems are shown in Sec. III D. Properties of the vortex core are discussed in Sec. III E. Finally, a summary of the work is presented in Sec. IV.

II. METHODS

Previous simulations of vortices in 3D bosonic systems, such as ^{4}He, have often employed a periodic array of counter-rotating vortices, which enables the usage of periodic boundary conditions. In the ^{4}He calculations of Ref. [32], the simulation cell consisted of 300 particles in four counter-rotating vortices. If we had employed a similar methodology, we would need the same number of fermion pairs, i.e., a system with 600 fermions. There are simulations of fermionic systems that have been performed with this number of particles, but the variance required for a detailed optimization is beyond the scope of this work. Instead, we considered a disk geometry similar to the one used in Ref. [33] for DMC simulations of the vortex core structure properties in ^{4}He.

A. Finite-size systems

We are interested in the interacting many-body problem, but it is useful to first consider the noninteracting case. In this

*lucas.madeira@asu.edu

 ©2017 American Physical Society

section we compare the energy of finite-size 2D systems to the results in the thermodynamic limit.

First let us consider the case of N fermions in a square of side L with periodic boundary conditions. The single-particle states are plane waves $\psi_{\mathbf{k_n}}(\mathbf{r}) = e^{i\mathbf{k_n}\cdot\mathbf{r}}/L$, with wave vector

$$\mathbf{k_n} = \frac{2\pi}{L}(n_x\hat{\mathbf{x}} + n_y\hat{\mathbf{y}}). \tag{1}$$

The eigenenergies are $E_\mathbf{n} = \hbar^2\mathbf{k}_\mathbf{n}^2/2m$, where m is the mass of the fermion. At $T = 0$, all states with energy up to the Fermi energy $\epsilon_F = \hbar^2 k_F^2/2m$, where k_F is the Fermi wave number, are occupied. A shell structure arises from the fact that different combinations of n_x and n_y in Eq. (1) yield the same $|\mathbf{k_n}|$. The closed shells occur at total particle number $N = (2,10,18,26,42,50,58,\ldots)$. The free gas energy of a finite system with N fermions, $E_{FG}^{\text{bulk}}(N)$, is readily calculated by filling the lowest energy states described by Eq. (1). In the thermodynamic limit, which corresponds to $N,L \to \infty$ and $n = N/L^2$ held constant, the energy per particle of the free gas is $E_{\text{FG}} = \epsilon_F/2$ and $k_F = \sqrt{2\pi n}$.

Now let us consider the case of N fermions in a disk of radius $\mathcal{R}$ with a hard wall boundary condition, i.e., the wave function must vanish at $\mathcal{R}$. The single-particle states are

$$\psi_{\nu p}(\rho,\varphi) = \mathcal{N}_{\nu p} J_\nu\left(\frac{j_{\nu p}}{\mathcal{R}}\rho\right)e^{i\nu\varphi}, \tag{2}$$

where (ρ,φ) are the usual polar coordinates, $\mathcal{N}_{\nu p}$ is a normalization constant, J_ν are Bessel functions of the first kind, and $j_{\nu p}$ is the pth zero of J_ν. The quantum number ν can take the values $0,\pm1,\pm2,\ldots$ and $p = 1,2,\ldots$. The corresponding eigenenergies are

$$E_{\nu p} = \frac{\hbar^2}{2m}\left(\frac{j_{\nu p}}{\mathcal{R}}\right)^2. \tag{3}$$

This system also presents a shell structure, due to the energy degeneracy of single-particle states with the same $|\nu|$, with shell closures at total particle number $N = (2,6,10,12,16,20,24,28,30,34,\ldots)$. Notice that the energy levels of the bulk system are much more degenerate than the ones of the disk. In practice this means that more shells are needed to describe a disk with a given N. The free gas energy for the disk, $E_{FG}^{\text{disk}}(N)$, can be calculated analogously to the bulk case using the energy levels of Eq. (3). The thermodynamic limit for this case corresponds to $\mathcal{R} \to \infty$ with $n = N/(\pi\mathcal{R}^2)$ held constant, and E_{FG} and k_F go to the same expressions as the bulk ones.

The comparison between the free gas energy of finite systems in the bulk case and in the disk geometry is not immediate due to the presence of hard walls in the latter. In order to compare the free gas energy in both geometries, we define

$$E_0^{\text{disk}}(N) = E_{FG}^{\text{disk}}(N) - \frac{\lambda_s}{2}\sqrt{\frac{n}{\pi N}}, \tag{4}$$

in which we separated the total energy $E_{FG}^{\text{disk}}(N)$ into a bulk component $E_0^{\text{disk}}(N)$, and a surface term, the second term on the right-hand side. For further discussions on the functional form of the surface term, see Sec. III A. Figure 1 shows $E_{FG}^{\text{bulk}}(N)$ and $E_0^{\text{disk}}(N)$, with $\lambda_s = 17.5\ E_{FG}k_F^{-1}$, at the same density. The value of λ_s, within a 0.2% error, was determined by fitting the data for $10 \leqslant N \leqslant 226$ to the functional form of Eq. (4).

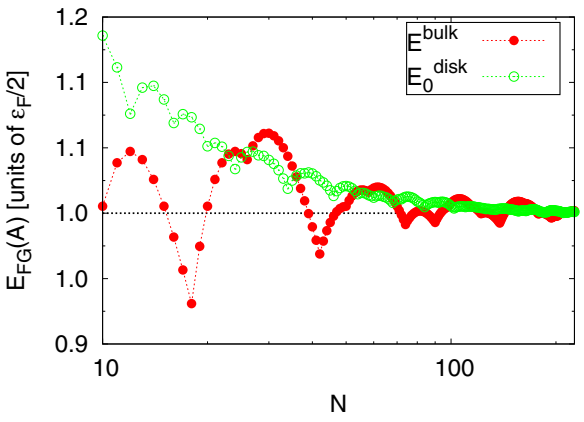

FIG. 1. Free gas energy for finite-size systems as a function of the number of particles N, where the dotted lines are drawn to guide the eye. The (red) closed circles denote the energy of the bulk system $E_{FG}^{\text{bulk}}(N)$, and the (green) open circles indicate the bulk energy component in the disk geometry $E_0^{\text{disk}}(N)$, as defined in Eq. (4). Local minima in $E_{FG}^{\text{bulk}}(N)$ correspond to shell closures.

The disk presents a considerably higher free gas energy, if compared to the bulk system, due to the presence of hard walls, but the difference between them is rapidly suppressed as we increase the particle number.

B. Scattering in 2D

Two-body scattering by a finite-range potential $V(r)$ in 2D is described by the Schrödinger equation. We separate the solutions into radial $R(r)$ and angular $P(\phi)$ parts, the latter being a constant for s-wave scattering. The two-body equation for an azimuthally symmetric (s-wave) solution is

$$\left[-\frac{\hbar^2\nabla^2}{2m_r} + V(r)\right]u(r) = \frac{\hbar^2k^2}{2m_r}u(r), \tag{5}$$

where m_r is the reduced mass of the system, and $\hbar^2k^2/2m_r$ is the scattering energy. The scattering length a and effective range r_{eff} can be easily determined from the $k \to 0$ solution of Eq. (5), $u_0(r)$, and its asymptotic form y_0. We choose the solution

$$y_0(r) = -\ln\left(\frac{r}{a}\right), \tag{6}$$

and we match u_0 and y_0, and their derivatives, outside the range of the potential.

In 2D, the low-energy phase shifts $\delta(k)$, a, and effective range r_{eff} are related by [34]

$$\cot\delta(k) \approx \frac{2}{\pi}\left[\ln\left(\frac{ka}{2}\right) + \gamma\right] + \frac{k^2r_{\text{eff}}^2}{4}, \tag{7}$$

where $\gamma = 0.577\ldots$ is the Euler-Mascheroni constant, and the effective range is defined as [35]

$$r_{\text{eff}}^2 = 4\int_0^\infty \left[y_0^2(r) - u_0^2(r)\right]r\,dr. \tag{8}$$

Equation (7) is often called the shape-independent approximation because it guarantees that a broad range of well-chosen potentials can be constructed to describe low-energy scattering. We consider the modified Poschl-Teller potential

$$V(r) = -v_0 \frac{\hbar^2}{m_r} \frac{\mu^2}{\cosh^2(\mu r)}, \tag{9}$$

where v_0 and μ can be tuned to reproduce the desired a and r_{eff}.

Bound states occur for purely attractive potentials for any strength in 2D. If we continually increase the depth of $V(r)$, a will eventually reach zero, and then it diverges to $+\infty$ when a new bound state is created. The binding energy of the pair is given by

$$\epsilon_b = -\frac{4\hbar^2}{ma^2 e^{2\gamma}}. \tag{10}$$

We chose values of v_0 and μ such that only one bound state is present, and $k_F r_{\text{eff}}$ is held constant at 0.006 [13]. This choice guarantees that the systems studied in this work are in the dilute regime, since $r_0 \gg r_{\text{eff}}$, where $r_0 = 1/\sqrt{\pi n}$ is of order of the interparticle spacing.

C. Wave functions

The BCS wave function, which describes pairing explicitly, has been successfully used in a variety of strongly interacting Fermi gases systems, such as 3D [36] and 2D [13] bulk systems, vortices in the unitary regime [21], two-component mixtures [37,38], and many other systems. This wave function, projected to a fixed number of particles N (half with spin-up and half with spin-down), can be written as the antisymmetrized product [39]

$$\psi_{\text{BCS}}(\mathbf{R}, S) = \mathcal{A}[\phi(\mathbf{r}_1, s_1, \mathbf{r}_2, s_2)\phi(\mathbf{r}_3, s_3, \mathbf{r}_4, s_4)\ldots \phi(\mathbf{r}_{N-1}, s_{N-1}, \mathbf{r}_N, s_N)], \tag{11}$$

where $\mathbf{R}$ is a vector containing the particle positions $\mathbf{r}_i$, S stands for the spins s_i, and ϕ is the pairing function, which is given by

$$\phi(\mathbf{r}, s, \mathbf{r}', s') = \tilde{\phi}(\mathbf{r}, \mathbf{r}')[\langle s\ s'|\uparrow\downarrow\rangle - \langle s\ s'|\downarrow\uparrow\rangle], \tag{12}$$

where we have explicitly included the spin part to impose singlet pairing. The assumed expressions for $\tilde{\phi}$ depend on the system being studied (see Secs. II C 1, II C 2, and II C 3). Since neither the Hamiltonian or any operators in the quantities we calculate flip the spins, we adopt hereafter the convention of primed indexes to denote spin-down particles and unprimed ones to refer to spin-up particles. Equation (11) reduces to

$$\psi_{\text{BCS}}(\mathbf{R}, S) = \mathcal{A}[\phi(\mathbf{r}_1, s_1, \mathbf{r}_{1'}, s_{1'})\phi(\mathbf{r}_2, s_2, \mathbf{r}_{2'}, s_{2'})\ldots \phi(\mathbf{r}_{N/2}, s_{N/2}, \mathbf{r}_{N/2'}, s_{N/2'})], \tag{13}$$

where the antisymmetrization is over spin-up and/or spin-down particles only. This wave function can be calculated efficiently as a determinant [40].

In addition to fully paired systems, it is also possible to simulate systems with unpaired particles [36], described by single-particle states $\Phi(\mathbf{r})$. For q pairs, u spin-up, and d spin-down unpaired single-particles states, $N = 2q + u + d$, we can rewrite Eq. (13) as

$$\begin{aligned}\psi_{\text{BCS}}(\mathbf{R}, S) = \mathcal{A}[&\phi(\mathbf{r}_1, s_1, \mathbf{r}_{1'}, s_{1'})\cdots \\ &\phi(\mathbf{r}_q, s_q, \mathbf{r}_{q'}, s_{q'})\Phi_{1\uparrow}(\mathbf{r}_{q+1})\cdots \\ &\Phi_{u\uparrow}(\mathbf{r}_{q+u})\Phi_{1\downarrow}(\mathbf{r}_{(q+1)'})\cdots \\ &\Phi_{d\downarrow}(\mathbf{r}_{(q+d)'})].\end{aligned} \tag{14}$$

We also included a two-body Jastrow factor $f(r_{ij'})$, $r_{ij'} = |\mathbf{r}_i - \mathbf{r}_{j'}|$, which accounts for correlations between antiparallel spins. It is obtained from solutions of the two-body Schrödinger's equation

$$\left[-\frac{\hbar^2\nabla^2}{2m_r} + V(r)\right] f(r < d) = \lambda f(r < d), \tag{15}$$

with the boundary conditions $f(r > d) = 1$ and $f'(r = d) = 0$, where d is a variational parameter, and λ is adjusted so that $f(r)$ is nodeless. The total trial wave function is written as

$$\psi_{\text{T}}(\mathbf{R}, S) = \prod_{i,j'} f(r_{ij'})\psi_{\text{BCS}}(\mathbf{R}, S). \tag{16}$$

1. Bulk system

The assumed form of the pairing function for the bulk case is the same as Ref. [36],

$$\tilde{\phi}_{\text{bulk}}(\mathbf{r}, \mathbf{r}') = \sum_{n=1}^{n_c} \alpha_n e^{i\mathbf{k_n}\cdot(\mathbf{r}-\mathbf{r}')} + \tilde{\beta}(|\mathbf{r} - \mathbf{r}'|), \tag{17}$$

where α_n are variational parameters, and contributions from momentum states up to a level n_c are included. Contributions with $n > n_c$ are included through the $\tilde{\beta}$ function given by

$$\tilde{\beta}(r) = \begin{cases} \beta(r) + \beta(L - r) - 2\beta(L/2) & \text{for } r \leqslant L/2 \\ 0 & \text{for } r > L/2 \end{cases} \tag{18}$$

with

$$\beta(r) = [1 + cbr][1 - e^{-dbr}]\frac{e^{-br}}{dbr}, \tag{19}$$

where $r = |\mathbf{r} - \mathbf{r}'|$ and b, c, and d are variational parameters. This functional form of $\beta(r)$ describes the short-distance correlation of particles with antiparallel spins. We consider $b = 0.5\ k_F$, $d = 5$, and c is adjusted so that $\partial\tilde{\beta}/\partial r = 0$ at $r = 0$.

2. Disk

The pairing function for the disk geometry is constructed using the single-particle orbitals of Eq. (2). Each pair consists of one single-particle orbital coupled with its time-reversed state. This ansatz has been used before in the 3D system [21], a cylinder with hard walls, and the form presented here is analogous to that one if we disregard the z components. We supposed the pairing function to be

$$\begin{aligned}\tilde{\phi}_{\text{disk}}(\mathbf{r}, \mathbf{r}') = &\sum_{n=1}^{n_c} \tilde{\alpha}_n \mathcal{N}_{\nu p}^2 J_\nu\left(\frac{j_{\nu p}}{\mathcal{R}}\rho\right) J_\nu\left(\frac{j_{\nu p}}{\mathcal{R}}\rho'\right) e^{i\nu(\varphi-\varphi')} \\ &+ \bar{\beta}(\mathbf{r}, \mathbf{r}'),\end{aligned} \tag{20}$$

where the $\tilde{\alpha}_n$ are variational parameters, and n is a label for the disk shells, such that different states with the same energy are

associated with the same variational parameter. The $\bar{\beta}$ function is similar to $\tilde{\beta}$ employed in the bulk system, but we modify it to ensure the hard wall boundary condition is met,

$$\bar{\beta}(\mathbf{r},\mathbf{r}') = \begin{cases} \mathcal{N}_{01}^2 J_0\left(\frac{j_{01}\rho}{\mathcal{R}}\right) J_0\left(\frac{j_{01}\rho'}{\mathcal{R}}\right)[\beta(r)+\beta(2\mathcal{R}-r)-2\beta(\mathcal{R})] & \text{for } r \leqslant \mathcal{R} \\ 0 & \text{for } r > \mathcal{R}\,, \end{cases} \tag{21}$$

and β has the same expression as the bulk case [Eq. (19)].

3. Vortex

The vortex excitation is accomplished by considering pairing orbitals which are eigenstates of L_z with eigenvalues $\pm\hbar$. This is achieved by coupling single-particle states with angular quantum numbers differing by 1. In this case we used pairing orbitals of the form

$$\begin{aligned}\tilde{\phi}_{\text{vortex}}(\mathbf{r},\mathbf{r}') = \sum_{n=1}^{n_c} \bar{\alpha}_n \mathcal{N}_{\nu p}\mathcal{N}_{\nu-1;p} \\ \times \left\{ J_\nu\left(\frac{j_{\nu p}}{\mathcal{R}}\rho\right) J_{\nu-1}\left(\frac{j_{\nu-1;p}}{\mathcal{R}}\rho'\right) e^{i[\nu\varphi-(\nu-1)\varphi']} \right. \\ \left. + J_\nu\left(\frac{j_{\nu p}}{\mathcal{R}}\rho'\right) J_{\nu-1}\left(\frac{j_{\nu-1;p}}{\mathcal{R}}\rho\right) e^{i[\nu\varphi'-(\nu-1)\varphi]} \right\},\end{aligned} \tag{22}$$

where n is a label for the vortex shells, and $\bar{\alpha}$ are variational parameters. The largest contribution is assumed to be from states with the same quantum number p for the radial part [21]. Equation (22) is symmetric under interchange of the prime and unprimed coordinates, as required for singlet pairing.

The $\bar{\beta}$ function of Eq. (21) is not suited to describe the vortex state because it is an eigenstate of L_z with angular momentum zero. We tried different functional forms that had the desired angular momentum eigenvalue, but none of them resulted in a significant lower total energy. Thus we chose to employ only the terms in Eq. (22).

D. Quantum Monte Carlo

The Hamiltonian of the two-component Fermi gas is given by

$$H = -\frac{\hbar^2}{2m}\left[\sum_{i=1}^{N_\uparrow}\nabla_i^2 + \sum_{i=j'}^{N_\downarrow}\nabla_{j'}^2\right] + \sum_{i,j'} V(r_{ij'}), \tag{23}$$

with $N = N_\uparrow + N_\downarrow$, and $V(r_{ij'})$ given by Eq. (9). The DMC method projects the lowest energy state of H from an initial state ψ_T, obtained from variational Monte Carlo (VMC) simulations. The propagation, which is carried out in imaginary time τ, can be written as

$$\psi(\tau) = e^{-(H-E_T)\tau}\psi_T, \tag{24}$$

where E_T is an energy offset. In the $\tau\to\infty$ limit, only the lowest energy component Φ_0 survives,

$$\lim_{\tau\to\infty}\psi(\tau) = \Phi_0. \tag{25}$$

The imaginary time evolution is given by

$$\psi(\mathbf{R},\tau) = \int d\mathbf{R}' G(\mathbf{R},\mathbf{R}',\tau)\psi_T(\mathbf{R}'), \tag{26}$$

where $G(\mathbf{R},\mathbf{R}',\tau)$ is the Green's function associated with H. The Green's function contains two pieces: a diffusion term related to the kinetic operator, and a branching term related to the potential. We solve an importance-sampled version of Eq. (26) iteratively, using the Trotter-Suzuki approximation to evaluate $G(\mathbf{R},\mathbf{R}',\tau)$, which requires the time steps $\Delta\tau$ to be small. We circumvent the fermion-sign problem by using the fixed-node approximation, which restricts transitions across a chosen nodal surface [41]. Hence our estimates of energy expectation values are upper bounds.

We carefully optimized the trial wave function ψ_T, since it is used in three ways: an approximation of the ground state in the VMC calculations, as an importance function, and to give the nodal surface for the fixed-node approximation. The variational parameters [42] in Eqs. (17), (20), and (22) were determined using the stochastic reconfiguration method [43].

Expectation values of operators that do not commute with the Hamiltonian, for example, the current and density, were calculated using extrapolated estimators [44]

$$\langle\Phi|\hat{S}|\Phi\rangle \approx 2\langle\Phi|\hat{S}|\psi_T\rangle - \langle\psi_T|\hat{S}|\psi_T\rangle + O((\Psi-\psi_T)^2), \tag{27}$$

where we combine the results of VMC and DMC runs.

III. RESULTS

We define the interaction strength $\eta \equiv \ln(k_F a)$. Large values of η correspond to the BCS side of the crossover, while small η are on the BEC side. We probed $0.0 \leqslant \eta \leqslant 1.5$, which encompasses the crossover region (see Sec. III C). For all systems the number density is $n = N/(\pi\mathcal{R}^2)$, and $k_F = \sqrt{2N}/\mathcal{R}$.

A. Ground-state energy and size effects

We used the pairing function of Eq. (17), and $N = 26$, to calculate the ground-state energy per particle of the bulk systems. Our results (see Table I) are in agreement with previous DMC calculations [13].

TABLE I. Comparison between the ground-state energy per particle of the bulk (E_{bulk}) and disk systems as a function of the interaction strength η. The parameters E_0 and λ_s [see Eq. (28)] are related to our assumption of the functional form of the ground-state energy per particle in the disk geometry.

η	$E_{\text{bulk}}\ E[_{FG}]$	$E_0\ E[_{FG}]$	$\lambda_s\ E\left[_{FG}k_F^{-1}\right]$
0.00	–2.3740(3)	–2.32(3)	6(2)
0.25	–1.3316(3)	–1.31(3)	8(2)
0.50	–0.6766(2)	–0.65(2)	8(1)
0.75	–0.2562(2)	–0.25(2)	11(1)
1.00	0.0233(2)	0.03(1)	11(1)
1.25	0.2149(2)	0.22(2)	12(1)
1.50	0.3523(2)	0.34(1)	13(1)

Previous DMC simulations of 2D Fermi gases found that $N = 26$ is well suited to simulate bulk properties of systems in the region studied here [13]. However, the disk geometry presents more intricate size-dependent effects. We investigated how the ground-state energy depends on the disk radius $\mathcal{R}$. In the thermodynamic limit, $\mathcal{R} \to \infty$, the energy per particle should go to the bulk value. Since our system has hard walls, the energy has a dependence on the "surface" of the disk. Including this surface term, the energy per particle can be fit to

$$E_{\rm disk}(\mathcal{R}) = E_0 + \frac{\lambda_s}{2\pi\mathcal{R}}, \tag{28}$$

where E_0 and λ_s are constants related to the bulk and surface terms, and $\lambda_s/(2\pi\mathcal{R})$ can be viewed as a surface tension.

A few words about Eq. (28) are in order. The relation between the thermodynamic properties of a confined fluid and the shape of the container where it is confined has been an active field of study. Our choice was inspired by functional forms (see, for example, Ref. [45]) where, aside from the constant term, thermodynamical properties are expressed as functions of the various curvatures of the container. The next correction to this functional form of the energy per particle would include a term proportional to $\mathcal{R}^{-2}$. We found that the inclusion of such a term does not significantly improve our description of the ground- state energy.

In order to determine the number of particles necessary to simulate systems in the disk geometry, with controllable size effects, we performed simulations with $26 \leqslant N \leqslant 70$ and all particles paired, i.e., only even values of N. The dependence of E_0 with the system size was investigated by fitting our data using Eq. (28) for different intervals of $\mathcal{R}$ or, equivalently, different intervals of N.

We found that fitting the data for $58 \leqslant N \leqslant 70$ resulted in a good agreement between $E_{\rm bulk}$ and E_0, that is, we were able to separate the bulk portion of the energy from the hard wall contribution in the disk geometry. The resulting parameters of the fitting procedure are summarized in Table I, and Fig. 2 shows the energy per particle as a function of $\mathcal{R}$ for all interaction strengths studied in this work.

The E_0 values agree with the bulk energies within the error bars, except for $\eta = 0$ and $\eta = 0.5$ (however, the differences between the values are less than 2% and 4%, respectively). As it can be seen in Table I, the typical uncertainty in E_0 is of order 0.01 E_F, independent of the interaction strength. Thus the relative error can be quite large for systems where the absolute value of the bulk energy is small, as it is observed for $\eta = 1.0$. This is an improvement if compared to a similar DMC calculation in 3D [21], which used the same procedure to calculate the ground-state energy per particle of a unitary Fermi gas, where the discrepancy between the result and the known bulk value was ∼30%.

We point out that this method is not intended to be a precise calculation of the bulk energy of these systems. Instead, it is a way for us to determine the minimum number of particles needed to simulate systems in the disk geometry with controllable size effects. If we had naively assumed that the same number of particles used in bulk calculations would suffice, $N = 26$, then we simply could not rely on the results. In our simulations with $26 \leqslant N \leqslant 38$ the discrepancies between

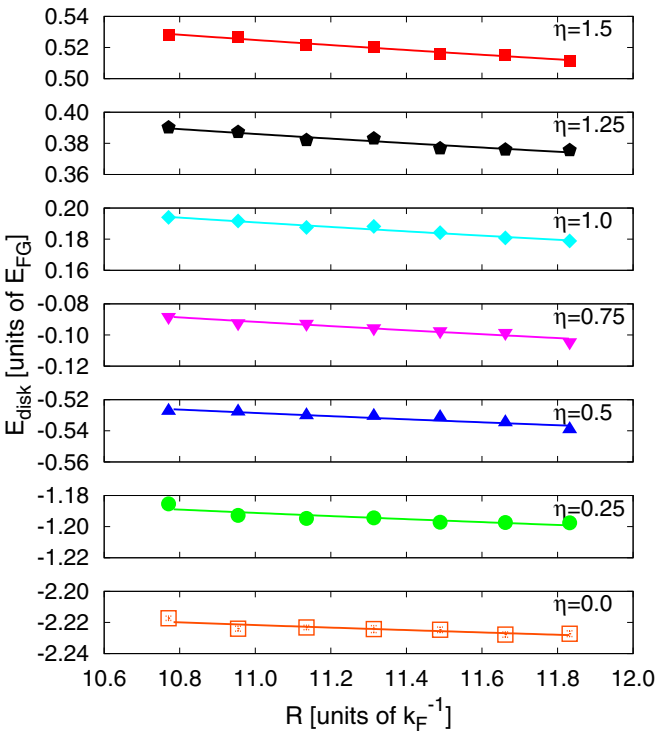

FIG. 2. Ground-state energy per particle $E_{\rm disk}$ as a function of the disk radius $\mathcal{R}$ for several interaction strengths. The curves correspond to the assumed functional form of Eq. (28), with the parameters given in Table I. Error bars are smaller than the symbols.

E_0 and $E_{\rm bulk}$ were as large as 50%, and in some cases the uncertainty in λ_s was bigger than the value itself. Results with $58 \leqslant N \leqslant 70$ are much more well-behaved, and they are within computational capabilities.

It is also noteworthy to mention that the energy contribution of the surface term, due to the presence of hard walls, is more significant for the BCS side than in the BEC limit (see the λ_s values in Table I). This is expected, since the largest energy contribution in the BEC side should be from the binding energy of the pairs [Eq. (10)], and they are smaller than the BCS pairs so that surface effects are smaller. One of our goals is to obtain the vortex excitation energy, which is the difference between the vortex and the ground-state energies. Since both systems have hard walls, we expect that the surface effects will tend to cancel.

B. Vortex excitation energy

The energy per particle of the vortex system is obtained using the pairing functions of Eq. (22). The vortex excitation energy is given by the difference between the energy of the vortex and ground-state systems, for the same number of particles. We performed simulations with $58 \leqslant N \leqslant 70$ and averaged the results.

In Fig. 3 we show the vortex excitation energy per particle as a function of the interaction strength. The energy necessary to excite the system to a vortex state increases as we move from the BCS to the BEC limit. The inset shows the vortex and ground-state energies per particle for $\eta = 1.5$, although

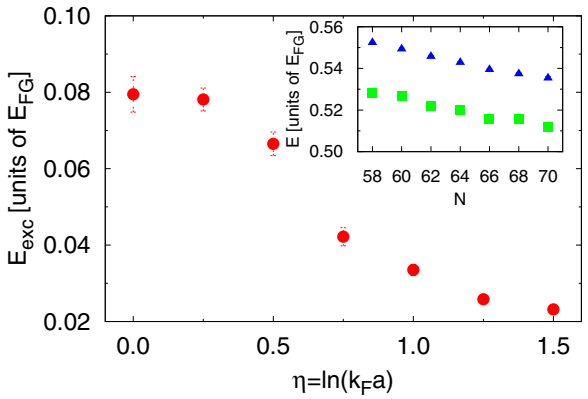

FIG. 3. Vortex excitation energy per particle $E_{\rm exc}$ as a function of the interaction strength η. The inset shows the ground-state (squares) and vortex (triangles) energies per particle as a function of the number of particles N for $\eta = 1.5$.

the other interaction strengths display the same qualitative behavior.

C. Crossover region

In 2D, the BCS limit corresponds to $k_F a \gg 1$ and the BEC limit to $k_F a \ll 1$; however, unlike 3D where the unitarity is signaled by the addition of a two-body bound state, there is no equivalent effect with the two-body sector in 2D. Nevertheless, we can determine the interaction strength for which we can add a pair to the system with zero energy cost. The chemical potential μ can be estimated as

$$\mu = \frac{\partial E}{\partial N}\bigg|_{\text{Even } N}, \tag{29}$$

for each interaction strength, where the even number condition implies that all particles are paired. For each value of η we used a finite difference formula to evaluate Eq. (29), for $58 \leqslant N \leqslant 70$ (see Fig. 4).

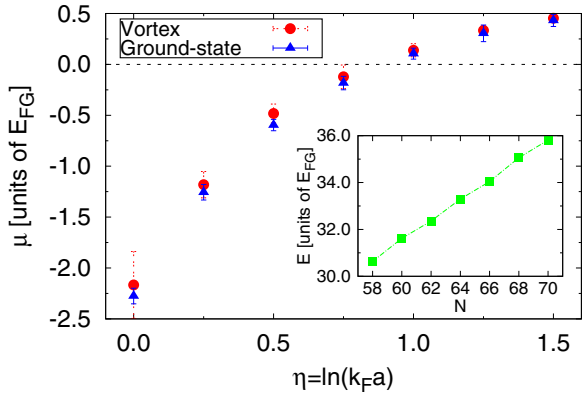

FIG. 4. Chemical potential of the ground state (triangles) and vortex (circles) as a function of the interaction strength. The chemical potential changes sign at $\eta \approx 0.90$ for the ground state and $\eta \approx 0.85$ for the vortex state. In the inset we show the total energy as a function of the number of particles for the ground state of $\eta = 1.5$. Other interaction strengths with positive (negative) μ have positive (negative) slopes.

We found that $\mu = 0$ at $\eta \approx 0.90$ for the ground state of the disk. Previous DMC simulations of 2D bulk systems [13] found that the chemical potential changes sign at $\eta \approx 0.65$. Although the results differ, most probably due to the different geometry employed in this work, it is safe to assume that the interaction strength interval $0 \leqslant \eta \leqslant 1.5$ encompasses the BEC-BCS crossover region. The chemical potential of the vortex state is higher than the ground state, as expected; thus $\mu = 0$ is at a smaller interaction strength, $\eta \approx 0.85$.

D. Density profile

We calculated the density profile $\mathcal{D}(\rho)$ along the radial direction ρ for both the vortex and ground-state systems. The normalization is such that

$$\int \mathcal{D}(\rho) d^2 r = 1, \tag{30}$$

where the integral is performed over the area of the disk. The results are obtained using the extrapolation procedure of Eq. (27), which combines both VMC and DMC runs. It is noteworthy to point out that although the densities observed in VMC and DMC simulations differ, they are much closer than previous results in 3D [21]. In that calculation it was needed to explicitly include a one-body term in the wave function to maximize the density overlap between DMC and VMC runs, whereas in this work no such term was employed.

Figure 5 shows the density profile of both the vortex and ground-state systems for $N = 70$ and $\eta = 1.5$. The oscillations in the density profiles are much more pronounced than in a similar DMC calculation of a unitary Fermi gas in 3D [21]. In this 3D calculation a cylindrical geometry was employed, with hard walls and periodic boundary conditions along the axis of the cylinder. The density profiles were obtained by averaging the results over the z direction of the axis of the cylinder; we therefore expect more fluctuations in 2D where the particles are confined to a plane. For the ground state, the density oscillations are surface effects. They are

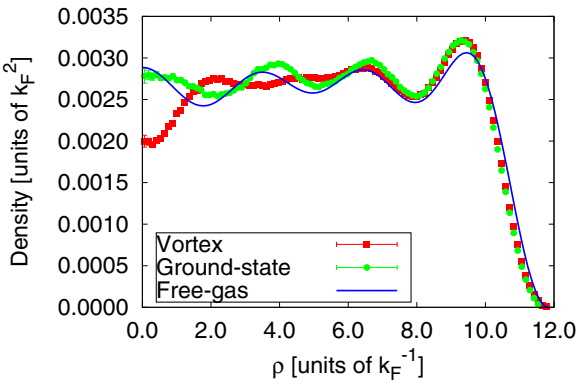

FIG. 5. Density profile along the radial direction ρ of the vortex (red squares) and ground state (green circles) for $N = 70$ and $\eta = 1.5$. Although there is a density suppression at the vortex core of ~30%, the density is nonzero at the center of the disk. We also plot the analytical result for the ground-state density of the free gas in a disk (blue curve), which presents oscillations due to the presence of hard walls.

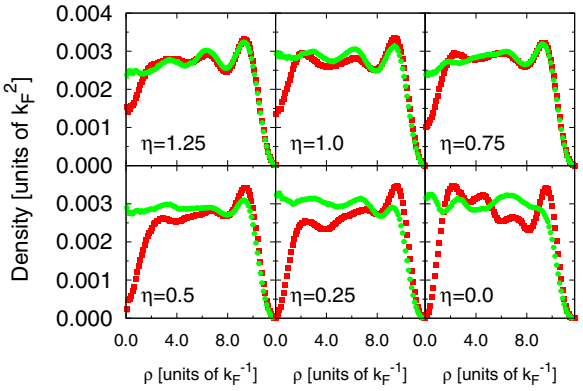

FIG. 6. Density profile along the radial direction ρ of the vortex (red squares) and ground state (green circles) for $N = 70$ and $0 \leqslant \eta \leqslant 1.25$. It is interesting to observe that the density at the vortex core diminishes as we go from the BCS to the BEC limit, and at $\eta \leqslant 0.25$ the core is completely depleted.

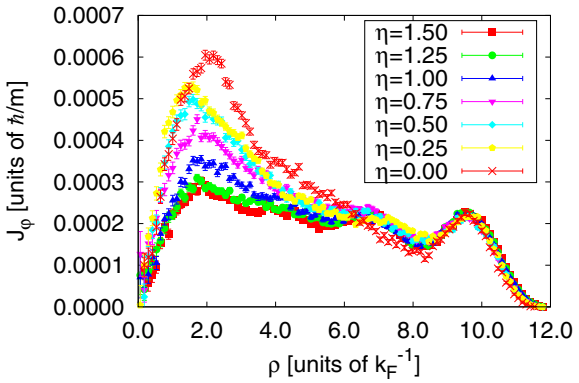

FIG. 7. Angular component of the probability current J_φ as a function of the radial coordinate ρ for several interaction strengths η. The position of its maximum provides an estimate of the vortex core size.

present in both the interacting and noninteracting systems, as it can be seen in Fig. 5.

In Fig. 6 we show the density profiles of the other interaction strengths studied in this work, $0 \leqslant \eta \leqslant 1.25$. We found that the density depletion at the vortex core goes from $\sim$30% at $\eta = 1.5$ to a completely depleted core at $\eta \leqslant 0.25$.

The regions close to the walls exhibit a characteristic behavior due to the hard wall condition we imposed, as it can be seen in Figs. 5 and 6. In order to estimate the number of particles outside this region, we can define the particle number a distance R from the center of the disk as

$$\mathcal{N}(R) = N \int_0^{2\pi} d\varphi \int_0^R d\rho\ \rho\ \mathcal{D}(\rho). \tag{31}$$

For the case of Figs. 5 and 6 where $N = 70$, if we set $R \approx 8\ k_F^{-1}$, $\mathcal{N}$ is approximately between 40 and 45 for the ground state and between 35 and 40 for the vortex systems. Hence the number of particles in this regime is larger than the usual value of $N = 26$ employed in bulk systems [13].

Additionally, we performed simulations of the vortex systems with an odd number of particles, i.e., one unpaired particle was added to a fully paired system, Eq. (14) with $q = 34$, $u = 1$, and $d = 0$. We set its angular momentum to zero, Eq. (2) with $\nu = 0$, and $p = 1$. In the BEC limit we observed a nonvanishing density at the center of the disk, which suggests that the unpaired particle fills the empty vortex core region. On the other hand, in the BCS limit the density close to the wall increased while the density at the origin was unchanged. We chose a qualitative discussion of this phenomenon because the required variance for a detailed optimization is beyond the scope of this work. Future calculations should include quantities such as the one-body density matrix, which may contribute to an accurate quantitative approach.

E. Vortex core size

The probability current density operator can be written as

$$\mathbf{J}(\mathbf{r}) = \frac{1}{2N} \sum_{j=1}^{N} [\mathbf{v}_j \delta^2(\mathbf{r} - \mathbf{r}_j) + \delta^2(\mathbf{r} - \mathbf{r}_j)\mathbf{v}_j], \tag{32}$$

where the velocity operator is $\mathbf{v}_j = \mathbf{p}_j/m \to -i\hbar\nabla_j/m$. We are interested in the angular component as a function of the radial coordinate $J_\varphi(\rho)$, because the position of its maximum can be used as an estimate of the vortex core size, $J_{\max} \equiv J_\varphi(\rho = \xi)$.

We followed the extrapolation procedure of Eq. (27). Figure 7 shows $J_\varphi(\rho)$ for $N = 70$ and $0 \leqslant \eta \leqslant 1.5$. The maximum of the current increases as we go from the BCS to the BEC limit, its value at the BEC side, $\eta = 0$, being more than twice $J_{\max}$ at the BCS side, $\eta = 1.5$. The position of the maximum is between $\xi = 1.7$ and $1.8\ k_F^{-1}$ at the BCS side of the crossover, i.e., $0.75 \leqslant \eta \leqslant 1.5$; at the BEC side, $\eta = 0.25$ and 0.5, $\xi \approx 1.6\ k_F^{-1}$. The case $\eta = 0$ moves away from the trend of a smaller core as we go from the BCS to the BEC limit, with $\xi = 2.0\ k_F^{-1}$. It is unclear if ξ or $J_{\max}$ depend on the disk radius $\mathcal{R}$, because the $\mathcal{R}$ values are closely spaced for $58 \leqslant N \leqslant 70$, and no significant difference was observed in the maximum as we varied N. Nevertheless, the relative results contribute to understanding how the vortex core evolves over the BEC-BCS crossover.

The wave function that we employed for the vortex state is an eigenstate of the total angular momentum operator. Since this operator commutes with the Hamiltonian, the diffusion procedure does not change the eigenvalue of the state. In addition, the calculation of the probability current density operator allowed us to verify that the vortex corresponds to a $N\hbar/2$ total angular momentum state in a straightforward way. The angular momentum can be written as

$$\mathbf{L} = m \int (\mathbf{r} \times \mathbf{J}) d^2\mathbf{r}, \tag{33}$$

and the component of interest is

$$L_z = 2\pi m \int \rho^2 J_\varphi(\rho) d\rho. \tag{34}$$

In our definition of the probability current density operator, we divide by the number of particles N [see Eq. (32)]. Thus the evaluation of L_z using Eq. (34) should yield $\hbar/2$. We verified that for all interaction strengths, this is in agreement with our simulations.

IV. SUMMARY

We have investigated several properties of vortices in 2D Fermi gases over the BEC-BCS crossover region. We dedicated a considerable portion of this work to carefully understand and control size effects in the disk geometry, since it is very convenient to simulating a single vortex. Given that we were interested in the evolution of the properties in the BEC-BCS crossover, determining the crossover region was important to verify that the interaction strengths studied in this work span the crossover.

The vortex excitation energies and the density profiles are quantities that can be compared with experiments, once they become available. Interestingly, the observed density depletion of the vortex core goes from $\sim$30% at the BCS side, $\eta = 1.5$, to an empty core for $\eta \leqslant 0.25$, at the BEC limit. In 3D, Bogoliubov–de Gennes theory has been used to calculate the density suppression at the vortex core throughout the BEC-BCS crossover [18–20]. Similar calculations in 2D could be compared to our findings [46]. Also, determining the probability current was essential to investigate the changes in the vortex core throughout the crossover region.

In 3D the interplay between experiments, theory, and simulations led to rapid advances in our comprehension of cold Fermi gases. Hopefully, our results will motivate experiments to increase our understanding of vortices in 2D Fermi gases.

ACKNOWLEDGMENTS

We would like to thank G. C. Strinati for useful discussions. This work was supported by the National Science Foundation under Grant No. PHY-1404405. This work used the Extreme Science and Engineering Discovery Environment (XSEDE), which is supported by National Science Foundation Grant No. ACI-1053575. The work of S.G. was supported by the NUCLEI SciDAC program, the US DOE under Contract No. DE-AC52-06NA25396, and the LANL LDRD program. This research used resources of the National Energy Research Scientific Computing Center, a DOE Office of Science User Facility supported by the Office of Science of the US Department of Energy under Contract No. DE-AC02-05CH11231.

[1] S. Giorgini, L. P. Pitaevskii, and S. Stringari, Rev. Mod. Phys. **80**, 1215 (2008).
[2] I. Bloch, J. Dalibard, and W. Zwerger, Rev. Mod. Phys. **80**, 885 (2008).
[3] M. Randeria, J.-M. Duan, and L.-Y. Shieh, Phys. Rev. Lett. **62**, 981 (1989).
[4] M. Randeria, J.-M. Duan, and L.-Y. Shieh, Phys. Rev. B **41**, 327 (1990).
[5] D. S. Petrov, M. A. Baranov, and G. V. Shlyapnikov, Phys. Rev. A **67**, 031601 (2003).
[6] J.-P. Martikainen and P. Törmä, Phys. Rev. Lett. **95**, 170407 (2005).
[7] J. Tempere, M. Wouters, and J. T. Devreese, Phys. Rev. B **75**, 184526 (2007).
[8] W. Zhang, G.-D. Lin, and L.-M. Duan, Phys. Rev. A **78**, 043617 (2008).
[9] K. Martiyanov, V. Makhalov, and A. Turlapov, Phys. Rev. Lett. **105**, 030404 (2010).
[10] A. A. Orel, P. Dyke, M. Delehaye, C. J. Vale, and H. Hu, New J. Phys. **13**, 113032 (2011).
[11] V. Makhalov, K. Martiyanov, and A. Turlapov, Phys. Rev. Lett. **112**, 045301 (2014).
[12] G. Bertaina and S. Giorgini, Phys. Rev. Lett. **106**, 110403 (2011).
[13] A. Galea, H. Dawkins, S. Gandolfi, and A. Gezerlis, Phys. Rev. A **93**, 023602 (2016).
[14] H. Shi, S. Chiesa, and S. Zhang, Phys. Rev. A **92**, 033603 (2015).
[15] E. R. Anderson and J. E. Drut, Phys. Rev. Lett. **115**, 115301 (2015).
[16] L. Rammelmüller, W. J. Porter, and J. E. Drut, Phys. Rev. A **93**, 033639 (2016).
[17] Z. Luo, C. E. Berger, and J. E. Drut, Phys. Rev. A **93**, 033604 (2016).
[18] A. Bulgac and Y. Yu, Phys. Rev. Lett. **91**, 190404 (2003).
[19] R. Sensarma, M. Randeria, and T.-L. Ho, Phys. Rev. Lett. **96**, 090403 (2006).
[20] S. Simonucci, P. Pieri, and G. C. Strinati, Phys. Rev. B **87**, 214507 (2013).
[21] L. Madeira, S. A. Vitiello, S. Gandolfi, and K. E. Schmidt, Phys. Rev. A **93**, 043604 (2016).
[22] M. W. Zwierlein, J. R. Abo-Shaeer, A. Schirotzek, C. H. Schunck, and W. Ketterle, Nature (London) **435**, 1047 (2005).
[23] V. L. Berezinskii, Sov. Phys. JETP **32**, 493 (1971).
[24] J. M. Kosterlitz and D. J. Thouless, J. Phys. C: Solid State Phys. **5**, L124 (1972).
[25] S. S. Botelho and C. A. R. Sá de Melo, Phys. Rev. Lett. **96**, 040404 (2006).
[26] J. Carlson, S. Gandolfi, and A. Gezerlis, in *Fifty Years of Nuclear BCS*, edited by R. A. Broglia and V. Zelevinsky (World Scientific Publishing Company, Singapore, 2013).
[27] A. Gezerlis and J. Carlson, Phys. Rev. C **77**, 032801(R) (2008).
[28] A. Gezerlis and J. Carlson, Phys. Rev. C **81**, 025803 (2010).
[29] F. V. De Blasio and O. Elgarøy, Phys. Rev. Lett. **82**, 1815 (1999).
[30] Y. Yu and A. Bulgac, Phys. Rev. Lett. **90**, 161101 (2003).
[31] D. G. Ravenhall, C. J. Pethick, and J. R. Wilson, Phys. Rev. Lett. **50**, 2066 (1983).
[32] M. Sadd, G. V. Chester, and L. Reatto, Phys. Rev. Lett. **79**, 2490 (1997).
[33] G. Ortiz and D. M. Ceperley, Phys. Rev. Lett. **75**, 4642 (1995).
[34] N. N. Khuri, A. Martin, J.-M. Richard, and T. T. Wu, J. Math. Phys. **50**, 072105 (2009).
[35] S. K. Adhikari, W. G. Gibson, and T. K. Lim, J. Chem. Phys. **85**, 5580 (1986).
[36] J. Carlson, S.-Y. Chang, V. R. Pandharipande, and K. E. Schmidt, Phys. Rev. Lett. **91**, 050401 (2003).
[37] A. Gezerlis, S. Gandolfi, K. E. Schmidt, and J. Carlson, Phys. Rev. Lett. **103**, 060403 (2009).
[38] S. Gandolfi, J. Phys.: Conf. Ser. **529**, 012011 (2014).
[39] J. P. Bouchaud, A. Georges, and C. Lhuillier, J. Phys. (Paris) **49**, 553 (1988).

[40] S. Gandolfi, A. Y. Illarionov, F. Pederiva, K. E. Schmidt, and S. Fantoni, Phys. Rev. C **80**, 045802 (2009).

[41] W. M. C. Foulkes, L. Mitas, R. J. Needs, and G. Rajagopal, Rev. Mod. Phys. **73**, 33 (2001).

[42] See Supplemental Material at http://link.aps.org/supplemental/10.1103/PhysRevA.95.053603 for the variational parameters of Eqs. (17), (20), and (22).

[43] M. Casula, C. Attaccalite, and S. Sorella, J. Chem. Phys. **121**, 7110 (2004).

[44] D. Ceperley and H. Kalos, in *Monte Carlo Methods in Statistics Physics Quantum Many-Body Problems*, edited by K. E. Binder (Springer-Verlag, Berlin, 1986), Vol. 7.

[45] P.-M. König, R. Roth, and K. R. Mecke, Phys. Rev. Lett. **93**, 160601 (2004).

[46] Recently, it was pointed out to us that pseudogap phenomena occurring in 2D and 3D Fermi gases can be related in a universal way through a variable that spans the BEC-BCS crossover [47]. Further studies are necessary to determine if this universality holds for other quantities such as the density and the probability current density per particle. This would provide a very clean way of comparing 2D and 3D results.

[47] F. Marsiglio, P. Pieri, A. Perali, F. Palestini, and G. C. Strinati, Phys. Rev. B **91**, 054509 (2015).